Langmuir
Article
pubs.acs.org/Langmuir
© 2010 American Chemical Society

Orientation and Self-Assembly of Cylindrical Particles by Anisotropic Capillary Interactions

Eric P. Lewandowski,[†] Marcello Cavallaro Jr.,[†,‡] Lorenzo Botto,[†] Jorge C. Bernate,[‡] Valeria Garbin,[†,†] and Kathleen J. Stebe*,[†]

[†]*Department of Chemical & Biomolecular Engineering, University of Pennsylvania, 220 South 33rd Street, Philadelphia, Pennsylvania 19104-6393, and* [‡]*Department of Chemical & Biomolecular Engineering, Johns Hopkins University, 3400 North Charles Street, Baltimore, Maryland 21218*

Received March 30, 2010. Revised Manuscript Received July 23, 2010

In this research, we study cylindrical microparticles at fluid interfaces. Cylinders orient and assemble with high reliability to form end-to-end chains in dilute surfaces or dense rectangular lattices in crowded surfaces owing to capillary interactions. In isolation, a cylinder assumes one of two possible equilibrium states, the end-on state, in which the cylinder axis is perpendicular to the interface, or the side-on state, in which the cylinder axis is parallel to the interface. A phase diagram relating aspect ratio and contact angle is constructed to predict the preferred state and verified in experiment. Cylinders in the side-on state create distortions that result in capillary interactions. Overlapping deformations by neighboring particles drive oriented capillary assembly. Interferometry, electron microscopy, and numerical simulations are used to characterize the interface shape around isolated particles. Experiments and numerics show that "side-on" cylinders have concentrated excess area near the end faces, and that the interface distortion resembles an elliptical quadrupole a few radii away from the particle surface. To model the cylinder interactions for separations greater than a few radii, an anisotropic potential is derived based on elliptical quadrupoles. This potential predicts an attractive force and a torque, both of which depend strongly on aspect ratio, in keeping with experiment. Particle trajectories and angular orientations recorded by video microscopy agree with the predicted potential. In particular, the analysis predicts the rate of rotation, a feature lacking in prior analyses. To understand interactions near contact, the concentrated excess area near the cylinder ends is quantified and its role in creating stable end-to-end assemblies is discussed. When a pair of cylinders is near contact, these high excess area regions overlap to form a capillary bridge between the particles. This capillary bridge may stabilize the end-to-end chains. Finally, on densely packed surfaces, cylinder-covered colloidosomes form with particles arranged in regular, rectangular lattices in the interface; this densely packed structure differs significantly from assemblies reported for colloidosomes or particle-stabilized droplets in the literature.

1. Introduction

Capillary attraction arises spontaneously between similar particles at fluid interfaces. The particles distort the interface and create excess surface area. When distortions from neighboring particles overlap, the area, and hence the energy, decreases if the particles migrate toward each other.[1] Capillary attraction between spherical microparticles in thin films is well understood[2−7] and widely exploited. Microspheres of diameters larger than the film create capillary interactions, which pull the particles into structures which form the nuclei of colloidal crystals.[8,9] Colloidal crystals are now routinely utilized as templates for polymeric and inorganic materials with controlled porosity for use in applications ranging from catalysis to separation technologies.[10−12] Microsphere assemblies are also used in diverse fields including photonics[13] and tissue engineering.[14,15]

Recent research in this area has focused on assembly of microparticles with negligible Bond number *Bo* at free surfaces.[16] In this limit, a smooth spherical particle with a uniform contact angle will immerse itself at a planar interface without distorting the interface, so no capillary interactions arise.[2] If, however, spherical particles have rough surfaces or patchy wetting, they can create an undulated contact line and assemble by capillary interactions even for $Bo \ll 1$.[7] Similarly, particles with a complex shape but constant surface energy also create contact line undulations.[17] Thus, shape alone, wetting heterogeneities, or a combination thereof can be used to create undulated contact lines and drive capillary assembly.

*Author to whom correspondence should be addressed. E-mail: (K.J.S.) kstebe@seas.upenn.edu.

(1) Danov, K. D.; Kralchevsky, P. A. *Adv. Colloid Interface Sci.* **2010**, *154*, 91−103.
(2) Binks, B. P. *Colloidal Particles at Liquid Interfaces*. Cambridge University Press: Cambridge, U.K., 2006.
(3) Danov, K. D.; Kralchevsky, P. A.; Naydenov, B. N.; Brenn, G. *J. Colloid Interface Sci.* **2005**, *287* (1), 121−134.
(4) Kralchevsky, P. A.; Denkov, N. D.; Danov, K. D. *Langmuir* **2001**, *17*, 7694−7705.
(5) Kralchevsky, P. A.; Nagayama, K. *Particles at Fluid Interfaces and Membranes: Attachment of Colloidal Particles and Proteins to Interfaces and Formation of Two-Dimensional Arrays*; Elsevier Science & Technology: Amsterdam, 2001.
(6) Oettel, M.; Dietrich, S. *Langmuir* **2008**, *24*, 1425−1441.
(7) Stamou, D.; Duschl, C.; Johannsmann, D. *Phys. Rev. E* **2000**, *62*, 5263−5272.
(8) Denkov, N. D.; Velev, O. D.; Kralchevsky, P. A.; Ivanov, I. B.; Yoshimura, H.; Nagayama, K. *Langmuir* **1992**, *8*, 3183−3190.
(9) Denkov, N. D.; Velev, O. D.; Kralchevsky, P. A.; Ivanov, I. B.; Yoshimura, H.; Nagayama, K. *Nature* **1993**, *361* (6407), 26−26.
(10) Gates, B.; Yin, Y. D.; Xia, Y. N. *Chem. Mater.* **1999**, *11*, 2827−2836.
(11) Holland, B. T.; Blanford, C. F.; Stein, A. *Science* **1998**, *281* (5376), 538−540.
(12) Jansen, J.; Stöcker, M.; Karge, H.; Weitkamp, J. *Advanced Zeolite Science and Applications*; Elsevier Science: Amsterdam, 1994; Vol. *85*.
(13) Colvin, V. L. *MRS Bull.* **2001**, *26*, 637−641.
(14) Cuddihy, M. J.; Kotov, N. A. *Tissue Eng., Part A* **2008**, *14*, 1639−1649.
(15) Yap, F. L.; Zhang, Y. *Biomaterials* **2007**, *28*, 2328−2338.
(16) For the microparticles studied, the Bond number $Bo = (\rho_L - \rho_V)gR^2/\gamma_{LV}$ represents the ratio of gravitational forces to surface tension forces. For small particles, around 10 μm or less, gravitational forces can usually be neglected.
(17) Brown, A. B. D.; Smith, C. G.; Rennie, A. R. *Phys. Rev. E* **2000**, *62* (1), 951-

The ability of capillary interactions to orient and assemble anisotropic particles in preferred configurations was first demonstrated in experiment by Bowden et al.[18] using finite Bond number, millimeter-scale complex shaped particles spread on a fluid interface. The particles were designed with complex shapes and surface energies to segregate and assemble in well-defined structures. This pioneering result demonstrated that capillary interactions can be used to assemble particles in configurations defined *a priori* by designing particle shape and wetting properties. Lucassen[19] anticipated that capillary interactions could arise at negligible *Bo* between particles with complex contact lines in an analytical study. He modeled interactions between parallel plates spanning an interface with pinned contact lines; the contact lines were described as Fourier modes of given wavelength. The interfacial distortion decayed exponentially with distance from the walls, with a decay length equal to the wavelength of the Fourier mode. The area of the interface was a minimum if the contact lines on both plates had the same wavelength and amplitude and were in phase. From this result, Lucassen argued that particles should approach with their features in registry, a concept later explored in experiment by Lewandowski et al.[20]

Capillary interactions between microparticles at free surfaces are currently studied as a potentially powerful means of directing particle orientation, assembly and rheology.[17−31] Research in the field can be divided roughly into two groups; the first group considers weak departures from circular contact lines, the other considers elongated particles which create highly noncircular contact lines. The numerical and analytical studies in the first group use multipole expansions in polar coordinates (r,θ) appropriate for contact lines that are weakly perturbed from circular contours.[1,3,7,17,29,30] Experiments in this group include studies of bent, circular metal particles[17] or microspheres with surface heterogeneities.[7] Numerics and experiments in the second group primarily address ellipsoidal particles at fluid interfaces.[21,22,25−28,31] The contributions of each group are summarized briefly in the following two paragraphs to place the current research in context.

To our knowledge, purely shape-driven capillary assembly at the microscale was first reported by Brown et al.,[17] who lithographically fabricated thin circular metal particles which bent when released from their template. When placed in an interface, the bent particles deformed the interface and assembled either in aggregates or in chains; the aggregation was attributed to quadrupolar distortions of the interface and the chaining was attributed qualitatively to higher order modes. Stamou et al.[7] provided an analytical basis for capillary attraction on the microscale in a study of undulated contact lines owing to chemical heterogeneities or surface roughness on spherical particles in an otherwise planar interface. Assuming small slopes, they identified the far field deformation as a quadrupole in a polar coordinate system, and derived the pair potential of interaction between two such quadrupoles. The resulting pair potential predicts attraction. Particles are predicted to orient with equal and opposite "bond angles". This mirror symmetric alignment is driven by a relatively long-range torque which goes as r_{12}^{-4}. Notably, however, no particular orientation is selected by this potential. In the text, the authors allude to preferred orientation arising from simultaneous action of quadrupolar and higher order modes. Kralchevsky and collaborators[1,3] extended Stamou's analysis to address pairwise interactions for multipoles of arbitrary order. Fournier et al.[30] numerically studied interactions among particles described by superposition of several modes, demonstrating that simultaneous quadrupolar−quadrupolar and octopolar−quadrupolar interactions give preferred alignments, and that nonpairwise interactions can lead to low energy assemblies. Finally, Van Nierop et al.[29] derived expressions for interaction potential between a pair of weakly elliptical particles. The particles had no preferred orientation, as in Stamou's analysis, and aspect ratio dependence was isolated in the prefactor. These authors also simulated the assembly of many particles; they report different configurations depending upon the stickiness of particle interactions upon contact.

The second group of studies addresses prolate ellipsoidal particles at fluid interfaces. Ellipsoidal particles create deformation fields at interfaces dominated by the particle shape. In experiment, the ellipsoids, made by stretching polystyrene microspheres, also present complex contact angles whose mean values vary with aspect ratio.[25,26] On dilute interfaces, ellipsoids assembled to form chains by capillarity, with the preferred orientation being material dependent; polystyrene ellipsoid formed chains oriented tip-to-tip, while ellipsoids coated with a silica shell oriented side-to-side.[25] The dynamics of tip-to-tip assembly (in terms of rate of approach) agreed with the pair potential derived by Stamou,[7] while side-to-side assembly deviated significantly from these predictions. Lehle et al.[22] study pair interactions of ellipsoids using analysis and numerics. Using analysis, they define a projected location for the unknown contact line to be an ellipse with eccentricity depending on the contact angle and eccentricity of the ellipsoid. Adopting a multipole expansion in elliptical modes, they numerically solve for the surface deformation and resulting forces of interaction between ellipsoids of a given aspect ratio. These simulations predict that identical ellipsoids should assemble tip-to-tip for center to center distance r_{12} larger than particle length, and side-to-side on closer approach.[22] Ellipsoids with slight mismatches in dimension or aspect ratio form "capillary arrows", in which they assemble with some finite angle between their major axes. These experiments are supported with numerical simulations of the pair interactions, which predict the observed orientation.[27] Networks of elliptical particles compressed at air−water[21,28] and oil−water[28] interfaces have been studied. Predominantly tip-to-tip assemblies are reported, as are jamming, buckling, and reorientation events. Ellipsoid-laden interfaces are highly elastic in comparison to spherical particle networks with similar dimensions and surface chemistry,[21,28] a property exploited in the creation of highly stable Pickering emulsions.[31] The preferred alignments captured numerically by Lehle imply torques beyond those predicted by Stamou which drive mirror symmetric alignment. As yet, to our knowledge, there is no analytical expression allowing the prediction of these torques and associated dynamics for eccentric particles such as ellipsoids or cylinders, and the existing numerical studies,[22,27]

(18) Bowden, N.; Terfort, A.; Carbeck, J.; Whitesides, G. M. *Science* **1997**, *276* (5310), 233−235. 960.
(19) Lucassen, J. *Colloids Surf.* **1992**, *65* (2−3), 131−137.
(20) Lewandowski, E. P.; Bernate, J. A.; Tseng, A.; Searson, P. C.; Stebe, K. J. *Soft Matter* **2009**, *5*, 886−890.
(21) Basavaraj, M. G.; Fuller, G. G.; Fransaer, J.; Vermant, J. *Langmuir* **2006**, *22*, 6605−6612.
(22) Lehle, H.; Noruzifar, E.; Oettel, M. *Eur. Phys. J. E* **2008**, *26*, 151−160.
(23) Lewandowski, E. P.; Bernate, J. A.; Searson, P. C.; Stebe, K. J. *Langmuir* **2008**, *24*, 9302−9307.
(24) Lewandowski, E. P.; Searson, P. C.; Stebe, K. J. *J. Phys. Chem. B* **2006**, *110*, 4283−4290.
(25) Loudet, J. C.; Alsayed, A. M.; Zhang, J.; Yodh, A. G. *Phys. Rev. Lett.* **2005**, *94*, 018301.
(26) Loudet, J. C.; Yodh, A. G.; Pouligny, B. *Phys. Rev. Lett.* **2006**, *97*, 018304.
(27) Loudet, J. C.; Pouligny, B. *EPL* **2009**, *85*, 28003.
(28) Basavaraj, M. Fransaer, J. Vermant, J. *Langmuir* **2009**, *25*, 2718−2728.
(29) van Nierop, E. A.; Stijnman, M. A.; Hilgenfeldt, S. *Europhys. Lett.* **2005**, *72*, 671−677.
(30) Fournier, J. B.; Galatola, P. *Phys Rev. E* **2002**, *65*, 031601.
(31) Basavaraj, M.; Vandebril, S., Fransaer, J., Vermant, J. *Softmatter* **2009** *5*, 1717−1727.

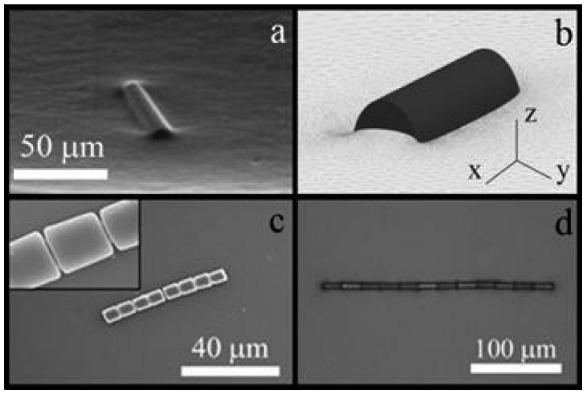

Figure 1. (a) Environmental SEM image of a right circular cylinder of SU-8 epoxy resin fixed in a gelled fluid interface for $\Lambda = 3$. (b) Surface Evolver simulation results for a right circular cylinder with aspect ratio $\Lambda = 3$ and contact angle $\theta_c = 80°$. (c and d) SEM images of chains of cylinders formed at aqueous-air interface by capillary attraction for aspect ratios Λ: (c) $\Lambda = 1.2$ and (d) $\Lambda = 2.5$.

while illuminating, have limited predictive value owing to the limited range of parameters considered.

This paper addresses two aspects of shape-driven capillary assembly.

First, we derive a pair potential for interacting elongated particles approximated as two elliptical quadrupoles. Notably, elliptical quadrupoles were the dominant mode in Lehle's numerical simulation of interacting ellipsoids. We will show in this work that they are also the dominant deformation mode around cylinders at interfaces, in that this mode quantitatively agrees with the exact interface deformation within a few radii of the cylinder surface. The analytical pair potential predicts forces, torques and preferred alignment in keeping with experiment. In particular, this pair potential predicts the dynamics of rotation, a feature not captured by prior analyses, as is confirmed by comparison to experiment.

Second, we use experiment, numerics and analysis to address the behavior of cylindrical particles in isolation, in pairwise interaction, and in dense assemblies. Cylinders differ significantly from ellipsoids. Alone, cylinders can orient end-on or side-on.[24] In the side-on orientation, cylinders deform the interface (Figures 1, parts a and b). This deformation is explored in detail with exact numerics from which we extract the leading order mode, the elliptical quadrupole. Deviations from this mode are significant near the ends of the cylinder. The implications of these local deformations are discussed for particles near contact. In interaction, cylinders assemble end-to-end.[20,23] This end-to-end assembly is highly robust and has been observed for every pairwise interaction recorded between cylinders on surfactant-free surfaces in our laboratory, including aqueous-air and aqueous-oil interfaces (Figure 1, parts c and d). This preference for end-to-end assembly is explained using our pair potential. On close approach, the interface forms a capillary bridge between the cylinders, which creates energy barriers to reorientation and stabilizes the end-to-end chains. Finally, on densely packed surfaces, cylinders form regular, rectangular lattices which differ significantly from assemblies reported for colloidisomes or particle-stabilized droplets in the literature.

2. Materials and Methods

Cylinders are fabricated from photoresist (SU-8 2000, Microchem) via contact lithography. SU-8 negative photoresist is spin-coated onto a silicon wafer and exposed with UV light (i-line) through a chromium mask (Microtronics Inc.). Cylinder length is determined by the thickness of the photoresist and cylinder radius by the lateral dimensions of the mask features. Particles are liberated by sonication in aqueous ethanol solutions (20% v/v) or by lift-off from a sacrificial layer of omnicoat or copper. Particles are then rinsed and stored in aqueous-ethanol solutions to be used within 4 weeks of preparation. SU-8 particles are partially wet with static contact angle $\theta_c = 80 \pm 2°$ as determined by a sessile drop on a planar macroscopic sample. Advancing and receding contact angles are $\theta_A = 95°$ and $\theta_R = 70°$, respectively.

Environmental SEM images are obtained for particles immobilized at a fluid interface using a gel trapping technique.[32] An aqueous solution containing 2 wt % of Kelcogel, a gellan gum (supplied by CPKelco), is prepared in deionized water (Millipore) heated to 95 °C. The gellan gum is centrifuged to release air bubbles, cooled to 50 °C, and poured into a Petri dish. Particles are spread onto this gellan solution−air interface from suspension in isopropanol using a 10 μL Hamilton gastight syringe in one injection. The solution is cooled for 30 min to fix the particles in place. The particle and interface shape are then imaged under an environmental SEM (FEI Quanta 600 FEM SEM).

SEM images of cylinder chains are obtained via a variation of the gel trapping technique discussed above. Cylinders are assembled at an air-gellan interface and subsequently cooled as previously stated. A polymer film comprised of a 10:1 mixture of PDMS Sylgard 184 Elastomer to curing agent (Dow Corning) is placed on top of the gel interface to create a negative replica of the interface. The polymer is centrifuged to release air bubbles, poured over the gellan gum and allowed to cure for 48 h at room temperature. The replica is cleaned by placing it in a 95 °C water bath for 5 min to rinse off excess gellan gum. Finally, a 2−3 nm layer of platinum is sputtered on the stamp for SEM preparation.

The interfacial deformation around particles trapped at liquid-fluid interfaces is visualized using interferometry.[33,26] We use reflection interference contrast microscopy to measure the interfacial topography around isolated cylinders. The beam from a diode-pumped solid state laser (λ = 532 nm) is collimated by a 10x microscope objective onto the particle-laden aqueous-air interface. Light reflected off the interface interferes with light reflected off the glass bottom of the dish (Fluorodish). The resulting interferograms are recorded on the camera sensor through the same objective. As the thickness of the aqueous subphase changes, the phase difference between the two beams also changes. The corresponding interferograms are recorded. The maximum phase shift (2π) is reached upon a change in thickness of one wavelength (532 nm). From sequences of interferograms with varying phase difference the three-dimensional interface shape is reconstructed through standard phase shifting techniques.[34] The height profile is obtained with a resolution better than 50 nm, and the lateral resolution is about 500 nm.

Pair interactions of particles are recorded by video microscopy (AxioImager M1m, AxioCam HSm). SU-8 particles are spread from aqueous ethanol solution (20% v/v) onto an aqueous subphase of pH 5.8 (Millipore). The particle orientation, dynamics of assembly, and the structure of the assemblies once formed are recorded by video microscopy at 60 fps and tracked using ImageJ software.

Numerical simulations are carried out using Surface Evolver, a simulation tool that has been extensively validated for problems involving capillary surfaces.[35] Surface Evolver is used here to find the surface minimizing the interfacial energy subject to boundary constraints under constant pressure conditions. The simulations with the cylinder in the side-on configuration presented in this paper were carried out for a fixed particle with a homogeneous Neumann condition imposed at the outer boundary of the computational domain. This boundary condition enforces a planar interface far from the particle. The condition of mechanical

(32) Paunov, V. N. *Langmuir* **2003**, *19*, 7970−7976.
(33) Hinsch, K. *J. Colloid Interface Sci.* **1983**, *92*, 243−255.
(34) Robinson, D. W.; Reid, G. T. *Interferogram Analysis*; Institute of Physics Publishing: England, 1993.
(35) Brakke, K. *Exp. Math.* **1992**, *1* (144).

equilibrium for the particle, at convergence, is automatically satisfied since the far field surface is free to move in the direction normal to the interface. (This is equivalent to allowing the height of the particle's center of mass to vary freely.) The validity of this approach was confirmed by simulating a neutrally buoyant sphere of radius R straddling an interface with a uniform contact angle θ_c. The known condition of mechanical equilibrium corresponding to a flat interface at height $R\cos\theta_c$ with respect to the sphere center was recovered.[2,36]

3. Results

3.1. Pair Potential between Elliptical Quadrupoles. In this section, we derive an analytical pair potential of interaction between elongated particles modeled as identical elliptical quadrupoles. The resulting pair potential predicts forces, torques and preferred alignments.

We adopt a particle-centered elliptical coordinate system (s,t), related to the Cartesian coordinate system (x,y) by the transformation

$$\begin{aligned} x &= \alpha\cosh(s)\cos(t) \\ y &= \alpha\sinh(s)\sin(t) \end{aligned} \tag{1}$$

where the x-axis is parallel to the major axis of the particle. In the (s,t) coordinates, $0 \le s < \infty$ and $0 \le t \le 2\pi$. Locii of constant s are ellipses with ratio of major to minor axis equal to $\coth(s)$. Lines of constant t are hyperbolae. The parameter α is a metric length scale related to distance from the origin that needs to be specified.

In the limit of zero Bond number, assuming a flat interface far from the particle, the interface shape h obeys Laplace's equation:

$$\nabla^2 h = 0 \tag{2}$$

Solutions of this equation respecting mechanical equilibrium in elliptical coordinates are decaying elliptical multipoles of which the slowest decaying mode is the elliptical quadrupole:[22]

$$h = H_e e^{-2(s-s_0)}\cos(2t) \tag{3}$$

Here, H_e is the amplitude of the interface deformation at the ellipse s_o. Far from the origin, $e^{-2s} \to (\alpha/r)^2/4$, and $t \to \theta$, (where r and θ are the usual polar coordinates), so the elliptical quadrupole decays asymptotically to the quadrupole in polar coordinates (r,θ):

$$h_{qp}(r,\theta) = H_p\left(\frac{R}{r}\right)^2\cos(2\theta) \tag{4a}$$

and therefore recovers the far-field deformation predicted by Stamou[7] for particles with contact line whose projection is a circle of radius R. The amplitude H_p of the polar quadrupole is thus related to H_e by:

$$H_p = \frac{H_e}{4}\left(\frac{\alpha}{R}\right)^2 e^{2s_0} \tag{4b}$$

The elliptical quadrupole reduces to the polar quadrupole for an elliptical contour s_0 of zero eccentricity. The pair potential we will derive based on elliptical quadrupoles will also smoothly recover the interactions between polar quadrupoles in the limit of large separations, and for eccentricity of unity.

(36) Chan, D. Y. C.; Henry, J. D.; White, L. R. *J. Colloid Interface Sci.* **1981**, *79*, 410−418.

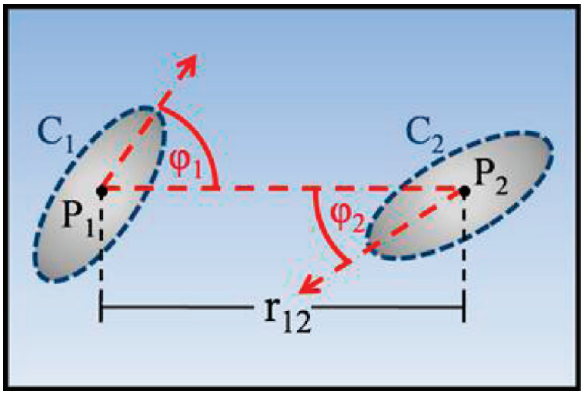

Figure 2. Schematic illustrating parameters used in calculation of E_{12}, the capillary interaction energy between elliptical quadrupoles 1 and 2. P_1 and P_2 denote the origin of two interacting elliptical quadruopolar disturbances. C_1 and C_2 denote the elliptical contours along which the elliptical quadrupole amplitude is H_e. The relative configuration is parametrized by the "bond" angles φ_1 and φ_2 and the center to center separation r_{12}.

The derivation of the pair potential between elliptical quadrupoles parallels that of Stamou for polar quadrupoles; the full derivation is stated here for clarity. Consider two identical particles, centered at P_1 and P_2, respectively, which create elliptical quadrupoles of magnitude H_e along the elliptical contours C_1 and C_2, as shown in Figure 2. The two centers are separated by a distance r_{12}; the line connecting P_1 and P_2 makes angles φ_1 and φ_2 with the major axes of C_1 and C_2, respectively. Introducing two elliptical coordinate systems, denoted (s_1,t_1) and (s_2,t_2) centered at P_1 and P_2, the contour C_1 is located at $s_1 = s_{01}$; the contour C_2 is located at $s_2 = s_{02}$. The interface deformation created by each particle is denoted:

$$\begin{aligned} h_1 &= H_e e^{-2(s_1 - s_{01})}\cos(2t_1) \\ h_2 &= H_e e^{-2(s_2 - s_{02})}\cos(2t_2) \end{aligned} \tag{5}$$

As in prior analytical work in the field,[1,7] we adopt the superposition approximation; i.e., we assume that the interface deformation can be approximated by:

$$h = h_1 + h_2 \tag{6}$$

In the small slope limit, the capillary energy, which is proportional to the area of the interface, is:

$$E = \frac{\gamma}{2}\int_{A_0}\nabla h\cdot\nabla h\,\mathrm{d}A \tag{7}$$

where the integral is taken over the region A_0 external to C_1 and C_2 and γ is the surface tension. Using eq 6, E can be recast:

$$E = \gamma\int_{A_0}\nabla h_1\cdot\nabla h_2\,\mathrm{d}A + \frac{\gamma}{2}\int_{A_0}\nabla h_1\cdot\nabla h_1\,\mathrm{d}A + \frac{\gamma}{2}\int_{A_0}\nabla h_2\cdot\nabla h_2\,\mathrm{d}A \tag{8}$$

The last two terms on the right-hand side are independent of r_{12}, φ_1 and φ_2, and thus do not determine the interaction energy. The cross-term involving h_1 and h_2, which we denote by E_{12}, represents the configuration-dependent interaction energy. By applying the divergence theorem to eq 8, and recalling eq 2, the interaction energy can be expressed in terms of line integrals over s_{01} and s_{02} only:[1,7]

$$E_{12} = -\gamma\int_{C_1} h_1\nabla h_2\cdot\vec{n}_1\,\mathrm{d}\ell - \gamma\int_{C_2} h_2\nabla h_1\cdot\vec{n}_2\,\mathrm{d}\ell \tag{9}$$

In this expression, $\vec{n}_1$ is the outward pointing normal to C_1, and $\vec{n}_2$ is the outward pointing normal to C_2. The expression for E_{12} does not contain contributions from the contour bounding A_0 at infinity, which are zero owing to the planar far field boundary condition. Since the disturbances at C_1 and C_2 are identical, the two line integrals appearing in eq 9 have the same numerical value. Thus, E_{12} can be expressed in terms of a line integral along only one of the two contours:

$$E_{12} = -2\gamma \int_{t_2=0}^{2\pi} h_2|_{s_{02}} \nabla h_1|_{s_{02}} \cdot \vec{n}_2 dl \cdot \qquad (10)$$

This integral can be considerably simplified by expanding ∇h_1 in a Taylor series about P_2,

$$\nabla h_1|_{s_{02}} \cong \nabla h_1|_{P_2} + \nabla\nabla h_1|_{P_2} \cdot \vec{r} \qquad (11)$$

where $\vec{r}$ is the position vector connecting each point on the contour s_{02} to its center P_1. Owing to the symmetries of the quadrupolar mode, the first term on the right-hand side of eq 11 does not contribute to the interaction energy, which can thus be written as:

$$E_{12} = -2\gamma \nabla\nabla h_1|_{P_2} : \int_{t_2=0}^{2\pi} h_2|_{s_{02}} \vec{r}\vec{n}_2 dl \qquad (12)$$

In this expression, the interaction energy E_{12} is given by the contraction of two tensors. The curvature tensor$\nabla\nabla h_1$ describes the curvature of the interfacial deformation h_1 at point P_2. The second tensor, the quadrupole moment tensor, is a weighted integral of h_2 along C_2. Complete expressions for these two tensors and the potential E_{12} are given in the Supporting Information.

The potential E_{12} is nonseparable; i.e., it cannot be expressed as the product of angle and distance dependent contributions. The exploration of the entire phase space on which E_{12} depends cannot be included in the limited space of the paper. Here we discuss the main features of the potential. To apply E_{12} to a particular system, three parameters must be specified. These include the length scale α, the parameter s_{02}, and the amplitude of the elliptical quadrupolar deformation H_e or, alternatively, H_p. (To stress the fact that the particles are identical, in the following we will use the symbol s_0 instead of s_{02}.) These parameters are, in general, functions of the particle geometry and wetting conditions.[37]

Here we apply E_{12} to a pair of cylindrical particles. To do so, we define the aspect ratio $\Lambda = L/2R$, where L is the particle length and R is the particle radius. The analysis of the exact interface topography around an isolated cylinder presented in section 3.2.3 indicates that the relationships

$$s_0 = \coth^{-1}(\Lambda) \quad \text{and} \quad \alpha = \sqrt{2}R\sqrt{\Lambda^2 - 1} \qquad (13)$$

are appropriate for cylindrical particles. These parameters correspond to an ellipsoid with major axis of length $\sqrt{2}(L)$. The energy and torque are discussed in normalized form, $E_{12}/\gamma H_p^2$ (Figure 3, Figure 4a) and

$$T/\gamma H_p^2 = -\frac{\partial}{\partial\varphi}(E_{12}/\gamma H_p^2)$$

(37) Appropriate values for these parameters for ellipsoidal particles, and a comparison of predicted interactions and Lehle's numerical predictions are presented in the Supporting Information.

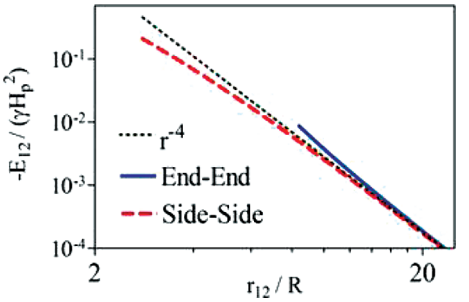

Figure 3. (a) Capillary energy E_{12} for interacting elliptical quadrupoles with $\Lambda = 3$. (Note the sign on the vertical axis). Solid and dashed curves terminate at "contact" which occurs at $r_{12} = \sqrt{2}(L)$ for quadrupoles approaching end-to-end, and $r_{12} = \sqrt{2}(R)$ for quadrupoles approaching side-to-side. L is the length of the corresponding cylinder. Solid blue curve: energy for end-to-end aligned elliptical quadrupoles, E_{12}^{ee}. Dashed red curve: energy for side-to-side aligned elliptical quadrupoles, E_{12}^{ss}. Black dotted curve: interaction energy between polar quadrupoles.

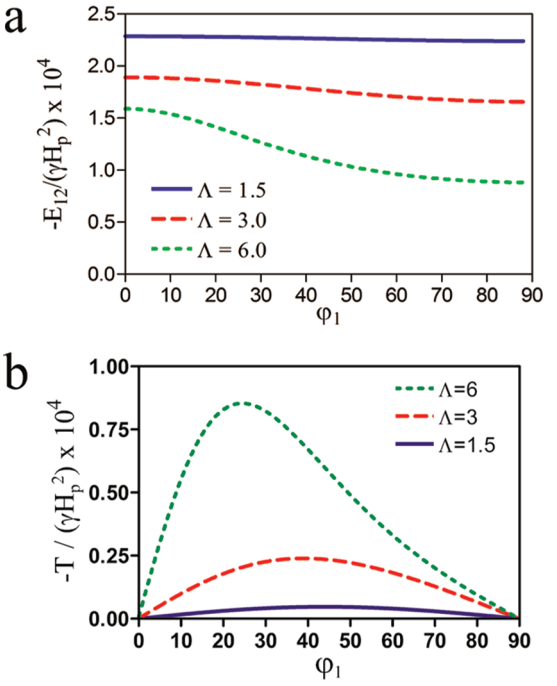

Figure 4. (a) Interaction energy $E_{12}/\gamma H_p^2$ and (b) torque $T/\gamma H_p^2$ for $r_{12}=20R$, assuming mirror symmetric orientations. These curves indicate that end-to-end assembly is favored. (Note the sign on the vertical axis.)

(Figure 4b). The interaction potentials for the end-to-end (E_{12}^{ee}) and side-to-side (E_{12}^{ss}) configurations are

$$E_{12}^{ee} = -f(\Lambda)\gamma \frac{1}{\tilde{r}^2(\tilde{r}+\sqrt{\tilde{r}^2-1})^2} \frac{\tilde{r}^2}{\tilde{r}^2-1}\left[2+\frac{\tilde{r}}{\sqrt{\tilde{r}^2-1}}\right] \qquad (14a)$$

$$E_{12}^{ss} = -f(\Lambda)\gamma \frac{1}{\tilde{r}^2(\tilde{r}+\sqrt{\tilde{r}^2+1})^2} \frac{\tilde{r}^2}{1+\tilde{r}^2}[2+\frac{\tilde{r}}{\sqrt{1+\tilde{r}^2}}] \qquad (14b)$$

where

$$f(\Lambda) = H_e^2\left[\frac{(\Lambda+1)^2}{(\Lambda-1)^2}-1\right]$$

$$= \left(\frac{4H_pR^2}{\alpha^2}\right)^2\left[1-\frac{(\Lambda-1)^2}{(\Lambda+1)^2}\right] \qquad (14c)$$

is a prefactor depending both on aspect ratio and on the quadrupolar amplitude and $\tilde{r} = r_{12}/\alpha$. In Figure 3, the interaction energy for the end-to-end (E_{12}^{ee}) and side-to-side (E_{12}^{ss}) configurations are compared. For $r_{12} > (2)^{1/2}L$ the end-to-end configuration is favored. Note that $r_{12} = (2)^{1/2}L$ corresponds to tip-to-tip contact of the ellipses circumscribing the two particles. For $r_{12} < (2)^{1/2}L$ however, the side-by-side configuration is favored. These alignments are enforced by a finite torque for all other orientations.

Thus, for $r_{12} > (2)^{1/2}L$ particles which are not aligned end-to-end experience a finite torque. This rotation represents significant, measurable deviations from the predictions of Stamou's potential for particles with $\Lambda \neq 1$.

For very large separations, the elliptical quadrupole tends to the polar quadrupole. In this limit, particles interact according to Stamou's potential, which requires that $\varphi_1 = -\varphi_2$. To explore the main features of E_{12} in configuration space ($r_{12},\varphi_1,\varphi_2$), it is therefore reasonable to consider $E_{12}/\gamma H_p^2$ as a function of φ_1 for $\varphi_2 = -\varphi_1$ and r_{12} fixed; this quantity is shown in Figure 4a for $r_{12} = 20R$ and several values of aspect ratio. For $\Lambda > 1$, the energy decreases monotonically reaching its minimum at $\varphi_1 = -\varphi_2 = 0$, which suggest that this configuration may be a global minimum for elongated particles at this separation.[38] The corresponding torque $T/\gamma H_p^2$ is shown for various aspect ratios in Figure 4b. The torque is a strong function of the aspect ratio. We discuss this dependence further in a consideration of asymptotic behavior of the potential, below. To explore the far-field behavior of this potential, we expand eqs 13 in powers of R/r_{12}:

$$E_{12}^{ss} \cong -12\pi\gamma H_p^2 4\frac{\Lambda}{(\Lambda+1)^2}\left(\frac{R}{r_{12}}\right)^4 + 40\pi\gamma H_p^2\left[4\frac{\Lambda}{(\Lambda+1)^2}\right](\Lambda^2-1)\left(\frac{R}{r_{12}}\right)^6 + \ldots \quad (15a)$$

$$E_{12}^{ee} \cong -12\pi\gamma H_p^2 4\frac{\Lambda}{(\Lambda+1)^2}\left(\frac{R}{r_{12}}\right)^4 - 40\pi\gamma H_p^2\left[4\frac{\Lambda}{(\Lambda+1)^2}\right](\Lambda^2-1)\left(\frac{R}{r_{12}}\right)^6 + \ldots \quad (15b)$$

where $H_p(\Lambda)$. To $O(r_{12}^{-4})$, side-to-side and end-to-end alignments have asymptotically identical interaction energies. To this order, the potential E_{12} with $\Lambda = 1$ corresponds to Stamou's potential. Differences in the energies for the two configurations appear at the next order, $O(r_{12}^{-6})$. These differences in energy create a torque, which is therefore also $O(r_{12}^{-6})$. An upper estimate for the magnitude of the torque on a pair of particles in a mirror-symmetric configuration is given by

$$T_{max} = \frac{E_{12}^{ss} - E_{12}^{ee}}{(\pi/2)}$$

The asymptotic analysis (eq 15) indicates that T_{max} is finite at any distance for $\Lambda \neq 1$, and decays as r_{12}^{-6} for large separations. This quantity is evaluated from eq 15, and shown as a function of r_{12} in Figure 5 for $\Lambda = 3$; the expected r_{12}^{-6} decay is apparent at large separations. In contrast, deviations in the *force* of interaction from Stamou's prediction occur at $O(r_{12}^{-7})$; these are weak contributions compared to the leading order terms, and manifest only on close approach.

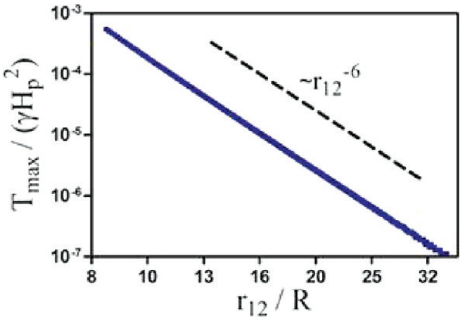

Figure 5. Maximum torque $T_{max}/\gamma H_p^2$ as a function of r_{12}/R, for $\Lambda = 3$ (blue line). The expected asymptotic behavior is recovered ($T_{max} \sim r_{12}^{-6}$) as shown by the black dashed line.

It is interesting to consider the behavior of E_{12} and T_{max} in the limit of large aspect ratio. For $\Lambda \to \infty$, $\alpha \sim \Lambda R = L/2$ and the magnitude of the elliptical quadrupole H_e saturates to a constant value; i.e., for long particles, the amplitude of the deformation becomes independent of length.[39] Using eqs 4b and 13, T_{max} in the far field is recast in terms of H_e and Λ:

$$T_{max} \sim \frac{H_e^2}{R^2}\frac{\Lambda(\Lambda^2-1)^3}{(\Lambda-1)^2}\left(\frac{R}{r_{12}}\right)^6 \quad (16)$$

For $\Lambda \to \infty$, this expression suggests a very strong asymptotical $T \sim \Lambda^5$ dependence.

3.2. Cylindrical Particles at Interfaces.

3.2.1. Interface topography near an Isolated Cylinder. An isolated right circular cylindrical particle located at an otherwise planar interface assumes one of two possible equilibrium orientations, depending upon the particle aspect ratio and contact angle θ_c. A cylinder can satisfy mechanical equilibrium in either an end-on orientation, in which the cylinder axis is perpendicular to the plane of the interface, or a side-on orientation, in which the axis is parallel to the plane of the interface. The orientation assumed by the cylinder at equilibrium is the one with the lower free energy. In the end-on orientation, the contact line pins along the circular edges of one of the planar faces and does not distort the interface. Partially wet cylinders ($\theta_c < 90°$) are completely submerged in the liquid phase, and have their top end attached to the interface, whereas partially nonwet cylinders ($\theta_c > 90°$) are totally enrobed in the vapor phase with their bottom face attached to the interface. Since the interface remains planar for the end-on configuration, the sum of the surface energies assumes a simple analytical expression. For side-on cylinders, however, the interfacial deformation is significant. The extent of the distortion depends on the particle wetting conditions and aspect ratio. Consequently, the equilibrium shape cannot be obtained analytically and we must rely on experiment and simulation.

An environmental SEM image for an SU-8 cylinder with $\Lambda = 3.0$ and $\theta_c = 80 \pm 2°$ located at an aqueous gellan-air interface is shown in Figure 1a. This figure qualitatively portrays key features common to the deformation field induced by cylinders for all the

(38) We have computed numerically several trajectories in phase space, such as that presented in section 3.3.2, from different initial interparticle separations and relative orientations. All these tests indicate that the potential admits only one minimum, corresponding to end-to-end alignment.

(39) In the limit of large Λ, Eq. 4b requires that H_p grow quadratically in Λ. In section 3.2.4, we extract H_p from the exact simulations of deformation fields around cylinders and show that (i) H_p indeed increases steeply with Λ and (ii) that H_e indeed saturates with Λ

aspect ratios and contact angles we have examined. We observe capillary rise at the flat end faces and a relatively weak downward deflection along the curved sides. These deformations decay with distance from the cylinder. Figure 1b depicts the interfacial topography around an isolated cylinder of aspect ratio $\Lambda = 3$ and $\theta_c = 80°$ as determined numerically. The simulation agrees qualitatively with the SEM image. The interface climbs the end-face, making an angle of exactly 80° with the vertical. The downward deflection along the cylinder side is weak, but must remain finite to satisfy mechanical equilibrium which requires that the sum of surface tension forces exerted by the interface along the three phase contact line be equal to zero.[20] This implies that the product of the mean slope of the interface along the end face times the diameter balance the product of the mean slope along the cylinder axis times the cylinder length. In dimensionless terms, as the aspect ratio increases, the slope along the major axis weakens, and the deformation field changes accordingly.

The exact topography is simulated as a function of contact angle and aspect ratio; contact line contours along the particle side and at the end-face are extracted for various θ_c and Λ. The contact angle dependence is shown in Figure 6, parts a and b for a cylinder with fixed aspect ratio ($\Lambda = 3$). These figures report the height h of the contact line with respect to the particle center-of-mass h_c, where, recall, the coordinate x lies along the cylinder major axis, with $x = 0$ located at the plane of symmetry at the particle midlength, and the coordinate y lies along the cylinder minor axis, with $h = 0$ corresponding to the height of the interface far from the particle. For $\theta_c = 90°$ the interface is flat and bisects the cylinder (not shown in the figure). As θ_c decreases, h_c decreases, thus, more of the cylinder is submerged. For $\theta_c \leq 60°$, the end face is covered with liquid (not shown), and the contact line pins at the top of the end-face. For intermediate contact angle, ($65° < \theta_c < 90°$), the difference between the maximum surface rise at the end-face, and the minimum surface depression along the cylinder side, increases with $\cos\theta_c$; i.e., the amplitude of the surface deformation increases with particle wetting. The interface topography also depends strongly on the particle aspect ratio. We explore this dependence for fixed $\theta_c = 80°$. Contact line contours along the particle end face are given in Figure 6c; those along the particle sides are given in Figure 6d. As Λ increases, the degree of immersion of the particle decreases, and the magnitude of the rise on the end face also decreases. Along the particle sides, becomes flatter with Λ; approaching $\cos(80°) = 0.1736$ for large Λ as expected for an infinitely long cylinder at zero Bo in a planar interface.[36]

3.2.2. Orientations of Isolated Cylinders. A phase diagram in (θ_c, Λ) parameter space can be defined with conditions for coexistence separating the end-on and side-on states. The coexistence curve is found by equating the free energies of these two orientations. The general expression for the free energy E of the system comprised of the particle and the liquid−vapor interface is

$$E = \gamma S_{lv} + \gamma_{sv} S_{sv} + \gamma_{ls} S_{ls} + \frac{g}{2}\int_A \Delta\rho_{lv} h^2 \, dA + \int_A \Delta P h \, dA + E_p \tag{17}$$

The contributions to the right-hand side of this expression include the sum of the surface energy contributions, where γ, γ_{sv}, and γ_{ls} denote the surface tensions between the liquid−vapor, solid−vapor, and liquid−solid phases and S_{lv}, S_{sv}, and S_{ls} are the respective surface areas; the gravitational potential energy of the liquid meniscus, where $\Delta\rho_{lv}$ is the density difference between the two fluids and h is the height of the interface defined with respect to the height of the planar interface far from the particle;

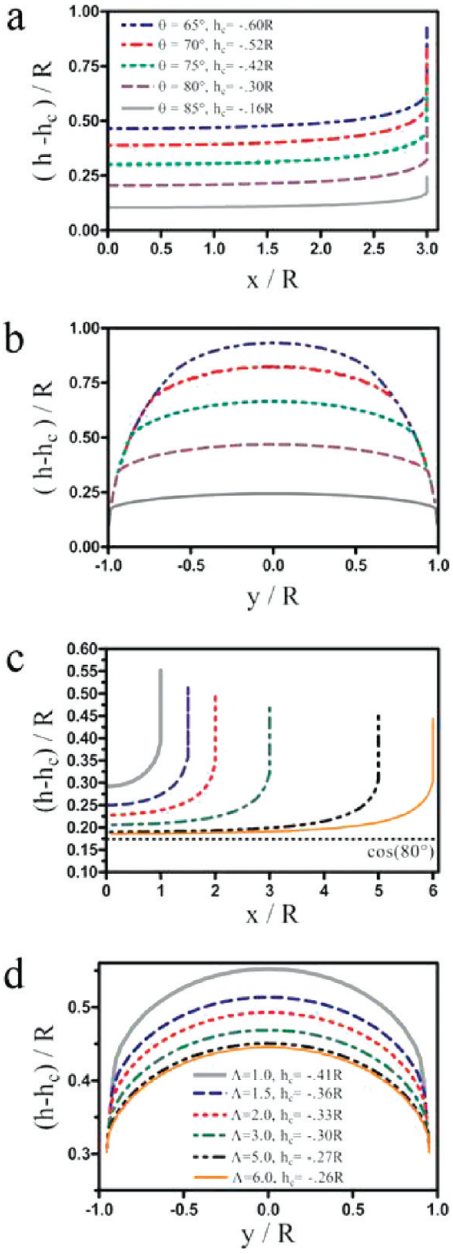

Figure 6. Contact line profiles for different contact angle θ_c for fixed aspect ratio $\Lambda = 3$: (a) along cylinder side; (b) along cylinder end face. Contact line profiles for different Λ for fixed $\theta_c = 80°$: (c) along cylinder side; (d) along cylinder end face.

the pV work, where ΔP indicates the pressure difference across the interface; and finally, the gravitational potential energy of the particle E_p. Since the gravitational force is negligible in comparison to the surface tension force in our system, i.e., Bond number $Bo \ll 1$, the terms involving gravity are negligible. The assumption of zero mean curvature implies that the pV work term is also zero. Thus, the free energy change between end-on and side-on orientations is governed solely by the sum of the surface energies. Calculation of the free energy for the end-on case is straightforward, as the fluid−fluid interface is flat and the contact line pins at one of the two end faces. In the side-on case, the surface energies associated with the equilibrium topography must be extracted from numerical simulations. The surface energies associated with these topographies are calculated and equated to the analytical expression for the end-on state to find points of coexistence. The results are plotted as green diamond shaped symbols in

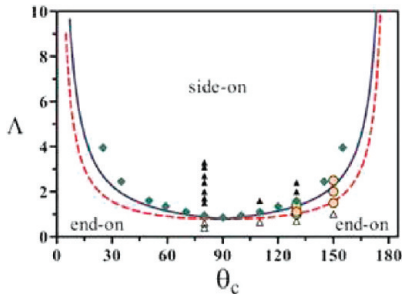

Figure 7. Phase diagram for isolated cylinders. A cylinder assumes an end-on state or a side-on state depending on Λ and θ_c. Green diamonds: points demarcating coexistence between the two states calculated from fully resolved simulations. Curves correspond to approximate analytical expressions accounting for liquid−vapor surface energy only (dashed red curve), and for liquid−vapor and liquid−solid surface energy (solid blue curve). Filled triangles: experimental data for particles observed in side-on state only; open triangles: particles observed in end-on state only. Yellow circles indicate particles for which both the side-on and end-on configurations are observed.

Figure 7. Owing to the symmetries of the wetting configurations in the zero gravity limit, the coexistence curve is symmetric about $\theta_c = \pi/2$.

Here, we compare this exact phase diagram to approximate expressions for the coexistence curve in order to identify the dominant surface energy contributions. The liquid−vapor energy term must be retained since particles attach to interfaces because the elimination of liquid−vapor interfacial area lowers the energy of the system.[2] As a first approximation, we neglect the deflections of the interface in the side-on state and assume that the elimination of liquid−vapor interface alone controls particle orientation. Under these assumptions, a cylinder can satisfy the contact angle boundary condition by creating a rectangular "hole" in the fluid interface of area $2LR \sin \theta_c$. This approximation is valid if θ_c is sufficiently close to 90°. We have verified that for $\theta_c = 80°$, the predicted reduction in liquid−vapor area caused by the particle is within 1% of the numerical result. For $\theta_c = 65°$, the corresponding error is less than 5%. End-on cylinders create a circular "hole" in the liquid−vapor interface of area πR^2. Equating the areas of the "holes" in the two states yields an approximate coexistence curve

$$\Lambda = \frac{\pi}{4}\frac{1}{\sin \theta_c}$$

shown as the dashed red curve in Figure 7. This curve captures the general trend of the numerical data, in particular for θ_c close to 90°. However, this crude approximation neglects the role of solid surface energies, which can be important for more wetting cylinders. In prior work, Lewandowski et al. had accounted for solid surface energies by approximating the end faces as completely wet for partial wetting cases, and completely nonwet for partially nonwetting cases.[24] According to Figure 6b, this approach is justified for $\theta_c < 60°$ and $\theta_c > 120°$ (for $\Lambda = 3$), while it is only approximate for $60° < \theta_c < 120°$, for which the wetted area fraction of the end face ranges from 0.5 to unity. Accounting for the solid surface energies gives the coexistence curve

$$\Lambda = \frac{\pi}{4}\frac{1-\cos \theta_c}{\sin \theta_c - \theta_c \cos \theta_c}$$

shown as the solid blue curve in Figure 7 (see Lewandowski et al.).[24] This approximation shows improved agreement with the exact results for relatively small contact angles. However, the crude approximation, based on liquid−vapor energy alone captures the overall trend of the numerical data reasonably well, suggesting that the elimination of liquid−vapor energy is the major factor in determining the preferred state.

The coexistence curves apply to any right circular cylinder with uniform surface energy at any fluid interface. We have performed experiments for various aspect ratio cylinders at aqueous−air and aqueous−oil interfaces. The experimental results are also reported in Figure 7 for particles with contact angles $\theta_c = 80°$, 110°, 130°, 150° and aspect ratio $0.25 \le \Lambda \le 4.0$. For each series of contact angle experiments, the radius is kept constant and the length is varied. Side-on configurations are shown as solid triangles while end-on configurations are hollow triangles. The data for $\theta_c = 80°$ were obtained using micrometer scale SU-8 epoxy resin cylinders ($R = 5\ \mu$m) spread from ethanol at aqueous-air interfaces. In previous work, the data for $\theta_c = 110°$ were obtained for octadecanethiol-functionalized Au nanowires (nominal $R = 120$ nm) at aqueous−air interfaces.[22] The data for $\theta_c = 130°$ were obtained for SU-8 cylinders ($R = 5\ \mu$m) at hexadecane−water interfaces. The data for $\theta_c = 150°$ were obtained for SU-8 cylinders ($R = 5\ \mu$m) at decanol−water interfaces. In these latter two sets of experiments, the particles were placed in the oil phase, settled under gravity and attached to the interface from solution in an adsorption-like process. Most of the experimental points obey the predicted phase diagram. However, in several cases, (indicated by the yellow circles on the figure) the microparticles adsorbed to the interface in both side-on and end-on orientations. Under these conditions, the end-on state was predicted to be the preferred configuration. We attribute the coexistence of both states to the trapping of the particles in a metastable state separated from the minimum energy configuration by a relatively large surface tension-induced energy barrier to reorientation. The observed orientation would then depend on the orientation of the cylinder when it initially contacts the interface. These issues have recently been considered by de Graaf[40,41] for cylindrical particles adsorbing to interfaces. Since the surface tension force scales as the square of the particle size, this effect is probably negligible for very small particles.

3.2.3. Division of Interfacial topography into Inner and Outer Domains. Quantitative Comparison of Experiment and Numerics. Interfacial deflections around a cylinder in a side-on orientation drive capillary interactions. Hence, we discuss the interfacial deformation field around isolated particles in greater detail for particles with $\theta_c = 80°$, the wetting condition for the majority of our experiments. Iso-height contours around a cylinder of aspect ratio $\Lambda = 2.5$ and contact angle 80° are shown in Figure 8a. The thick lines indicate zero-height contours, which separate regions of surface rise from regions of surface depression. At large distances from the cylinder corners (the point of intersection of the contact line with both the cylinder end faces and its curved sides), the iso-height contour lines reach an inclination of 45° with respect to either symmetry axis. Close to the cylinder corners this demarcation curve is almost parallel to the flat cylinder ends. Figure 8b shows interference fringes for an SU-8 microcylinder of the same aspect ratio and contact angle. The fringe pattern resembles the simulated deformation field. To compare the simulated and measured interfacial shapes quantitatively, surface height profiles are extracted from both the interference measurement and the simulation results along the major

(40) de Graaf, J., Dijkstra, M., van Roij, R. "Triangular tessellation scheme for the adsorption free energy at the liquid-liquid interface: Towards nonconvex patterned colloids" *Phys. Rev. E* **2009**, *80*, 051405.
(41) de Graaf, J., Dijkstra, M., van Roij, R. *J. Chem. Phys.* **2010**, *132*, 164902.

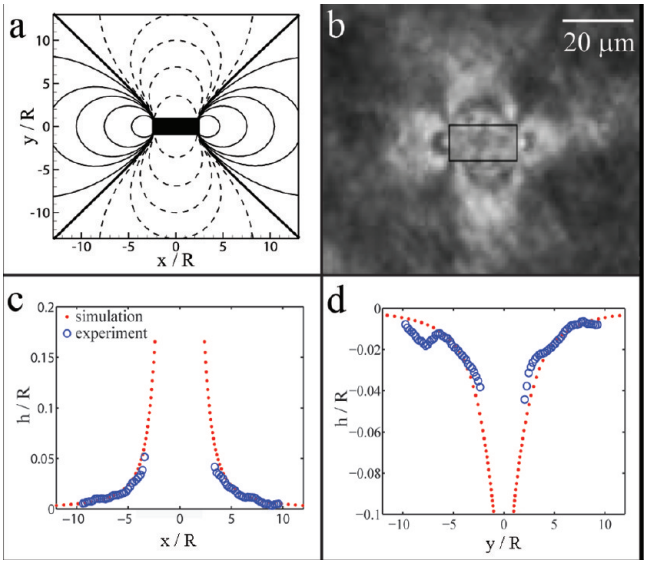

Figure 8. (a) Numerically simulated iso-height contours for a cylinder in the side-on state for $\Lambda = 2.5$ and $\theta_c = 80°$. The zero height contour is the bold black line. Thin solid contours demarcate region of height $h > 0$. Dashed contours demarcate regions of $h < 0$. (b) Interference fringes for SU-8 particle with $\Lambda = 2.5$ and $\theta_c = 80 \pm 2°$. (c and d) Comparison of surface height profiles extracted from interferograms (open blue circles) and from the simulation (red dotted lines) along the major and minor axes of the cylinder, respectively.

and minor axes of the cylinder and graphed in Figure 8, parts c and d, respectively. In these figures, experiment and numerics are compared for cylinders of the same aspect ratio. The numerical data are plotted up to the contact line. The experimental profile was truncated one particle radius from the contact line owing to noise in the interferometric images closer to the particle attributable to the limited NA of the imaging system. The profiles agree well, confirming that the deformation field can indeed be attributed to capillary effects and that the interface topography is governed by the particle shape and contact angle.

Outer Domain: The Elliptical Quadrupole. We divide the interfacial deformation field into two domains: an outer domain dominated by an elliptical quadrupolar mode of a particular eccentricity and magnitude, and an inner domain near the particle surface in which higher order modes contribute significantly. Interestingly, we will show that the outer domain is not a far field treatment. Rather, it applies to distances within a few radii of the particle surface. To do so, a particle-centered elliptical coordinate system (s,t) is adopted, related to the Cartesian coordinate system (x,y) by eq 1, where the x-axis is parallel to the cylinder's major axis. In this description, the ellipse with s_0 and αas specified in eq 13 is shown. Figure 9 depicts the corresponding elliptical quadrupolar deformation field. Only for these particular choices of s_0 and αdoes the ellipse circumscribe the cylinder, intersecting the cylinder at the points $x = \pm L/2, y = \pm R$, which we refer to as 'corners' of the cylinder. In Figure 9, we also chose a particular amplitude for the elliptical quadrupole $H_e = 0.083R$; this choice is not arbitrary, and will be justified below. For these special values of s_o, α, and H_e, the elliptical quadrupolar mode strongly resembles the exact solution for the interface topography. To facilitate quantitative comparison, this figure has the same contour level values as those used for Figure 8a, so that equal shape of the iso-contours means equal values of the interface elevation. In these figures, the bold line indicates the location and shape of the zero height contour traced by the hyperbola $t = \pi/4$, and asymptotically approaches an inclination of 45° with respect to either cylinder axis. This line, which divides regions of interface rise from depression, joins the cylinder "corners" in both figures. Capturing this feature is important, since the overall spatial distribution of rise and depression, for a given relative configuration of two interacting particles, determines the energy landscape.[1] The values for the interface heights for the exact simulation and the elliptical quadrupole are quite close for distances from the particle surface as small as few particle radii. For example, along the contour $s = 2.6s_0$, (within 3 radii of the particle surface), the maximum error in the area densities (defined in eq 18, below) is less than 8%. This error decreases steeply at larger distances. The elliptical quadrupole with these particular parameter values is adopted as the description for the interface shape in the outer domain.

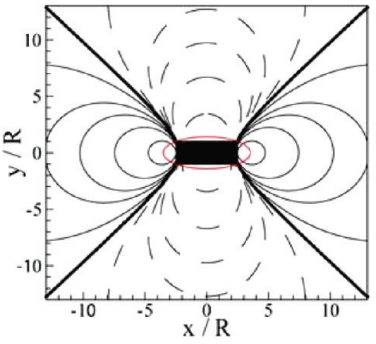

Figure 9. Elliptical quadrupolar deformation field (eq 3), for $\Lambda = 2.5$. The ellipse (shown in red) at $s = s_0$ for parameters defined in eq 13 intersects the corner points $x = \pm L/2$, $y = \pm R$. The thickened line indicates the zero height contour (obtained setting $t = \pi/4$). The amplitude of the quadrupole H_p corresponds to that of Figure 8a.

Inner Domain: Regions of High Area Density. A single mode cannot fully describe the complex interface shape very close the cylinder surface, where near field features arise owing to higher order multipoles and nonlinearities in the interface shape. To illustrate the importance of near-field features, the excess surface area density $\delta S/\delta S_0$ is calculated from fully resolved simulation data and compared to that calculated for an elliptical quadrupole in Figures 10a and b. The excess surface area density is defined as

$$\frac{\delta S}{\delta S_0} = (\sqrt{1 + \nabla h \cdot \nabla h} - 1) \qquad (18)$$

where $\delta S_0 = \delta x \delta y$ is the area of a planar interface element. The excess surface area density quantifies the local fractional increase in interfacial area over a planar reference state. Recalling that capillary energy is proportional to surface area, this can be considered as an energy density map.

In Figure 10, iso-area density contours are shown around a cylinder (Figure 10a, numerical simulation) and an elliptical quadrupole (Figure 10b, analytical expression) for $\Lambda = 2.5$. The dashed ellipse corresponds to $s = s_0$ and α as defined in eq 13. The contour level values selected in these figures correspond to identical surface excess area densities; the quantitative agreement in the outer domain is apparent. However, near the particle surface, significant differences emerge. The iso-area density contours for an elliptical quadrupole shown in Figure 10b roughly follow the shape of the ellipse $s = s_0$. The quantity $\delta S/\delta S_0$ attains a maximum value at the "tip" of the ellipse s_0. From eq 3, it can be shown that the excess surface area density within any s-constant ellipse is equally partitioned between regions with $h > 0$ and regions with $h < 0$. Examination of the

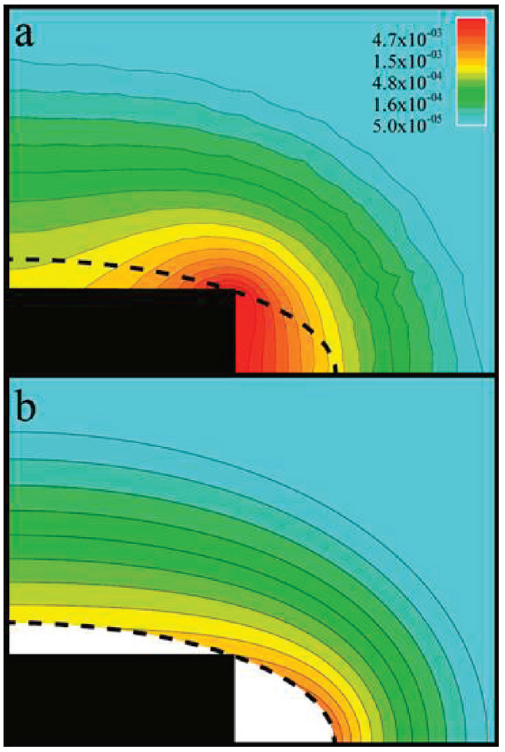

Figure 10. Excess surface area density $\delta S/\delta S_0$ (eq 18), for $\Lambda = 2.5$ and $\theta_c = 80°$: (a) around a cylinder from numerical simulation, with significant excess area density occurring along the cylinder end face, reaching its maximum at the corners; (b) surrounding an elliptical quadrupole from analytical expression. The maximum excess area density occurs at the "tip" of the dashed ellipse.

simulation results for the cylinder in Figure 10a reveals that the iso-area density contours roughly follow the shape of the planar end faces and bulge outward at the corners. The excess surface area density therefore varies only weakly along the contact line at the end face and reaches its maximum at the corner, where $\delta S/\delta S_0 \cong 0.026$. The excess area at the face midpoint $x = 2.5$R is

$$\delta S/\delta S_0 = \sqrt{1+1/\tan^2(\theta_c)} - 1 = 0.015$$

since the interface makes an angle of $\theta_c = 80°$ with the vertical end-face. The concentration of excess area near the cylinder surface is significant. We integrate to find the excess surface area of the interface between $s = 2.6s_0$ (an ellipse of major semiaxis $5.5R$, 3 radii longer than that of the particle) and the cylinder surface itself. The resulting excess surface energy is $0.042\gamma R^2$, which is on the same order of magnitude as that predicted by the elliptical quadrupole in the outer domain. Most of this energy (72%) is concentrated near the cylinder end face, where $h > 0$ and the surface gradients are steepest. This concentration near the end face becomes more significant for larger aspect ratios. For example, for $\Lambda = 5.0$ and $\theta_c = 80°$, approximately 88% of the excess surface area is concentrated in the region $h > 0$ within an ellipse of major semiaxis 3 radii longer than that of the particle. This feature is likely to be important for particle interactions near contact and the observed, highly stable end-to-end chaining. However, as this excess area is located so close to the particle, it cannot influence alignment and rotation at larger separations. We comment further on this hypothesis in Section 3.4.

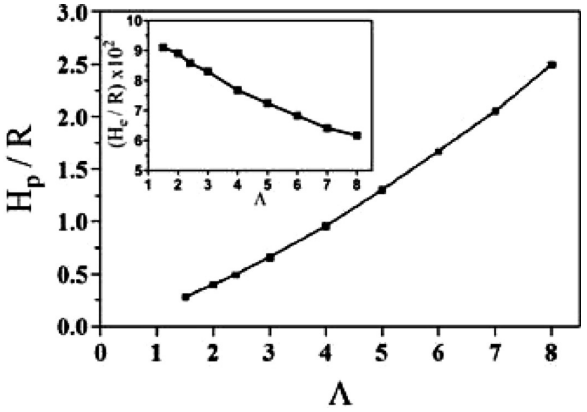

Figure 11. Amplitude of quadrupolar deformation mode versus Λ for $\theta_c = 80°$, extracted using eq 19 from the numerically simulated interface topography. (a) Polar quadrupole amplitude H_p. (b) Elliptical quadrupole amplitude H_e as defined in terms of H_p and Λ in eq 4b.

These discussions suggest that the inner domain can be roughly bounded by an ellipse of constant s slightly larger than the cylinder. For the range of aspect ratios considered here, an ellipse of major axis $\sim 3R$ larger than the cylinder length is selected as the bound to the inner domain. Beyond this region, i.e. in what we have called the outer domain, the elliptical quadrupole describes the deformation field reasonably well and can be used to understand particle interactions.

3.2.4. Amplitude of Quadrupoles from Exact Solution. Far from the cylinder, the interface topography decays to a polar quadrupole, as defined in eq 4. The magnitude H_p of this mode has been calculated from the simulated profile by computing the Fourier integral:

$$H_p = \frac{1}{\pi}\int_0^{2\pi} h(r,\theta) r^2 \cos 2\theta \, \mathrm{d}\theta \qquad (19)$$

along a circular contour surrounding the particle. (Since Fourier modes are orthogonal, the location of this contour is arbitrary, so long as it is selected outside of the region where nonlinearities play a role. H_p is computed at a distance greater than three radii from the particle surface.) The values of this coefficient are reported in Figure 11 as a function of aspect ratio for $\theta_c = 80$. H_p increases faster than linearly with Λ for a given particle radius R, reaching magnitudes well in excess of R. The magnitude of the deformation closer to the particle in the outer domain is characterized by the magnitude of the elliptical quadrupole H_e evaluated at s_o. This quantity is calculated from eq 4 and reported versus Λ as an inset to Figure 11. H_e appears to saturate at large aspect ratio, suggesting the magnitude of the interface deformation near the particle approaches a limiting value, and that undulations near the cylinder remain small compared to the cylinder radius R.

It remains to justify our particular choice of H_e in our definition of the elliptical quadrupole which describes the outer domain. For $\Lambda = 2.5$ and $\theta_c = 80$ (the conditions in Figure 8a), the value for H_p extracted from the simulation is $H_p = 0.50R$ (see Figure 11). According to eqs 4 and 13, this choice fixes $H_e = 0.083R$.

3.3. Pair Interactions Between Cylinders. *3.3.1. Experiment.* Trajectories of interacting pairs of cylinders were recorded at aqueous-air interfaces using video microscopy. From the sequential images, center to center distances r_{12} between the cylinders as a function of time t were extracted. At very large interparticle separations the cylinders attract each other, and the rotation is negligible with respect to the attraction (consistent with the torque decaying faster than the force). For these distances,

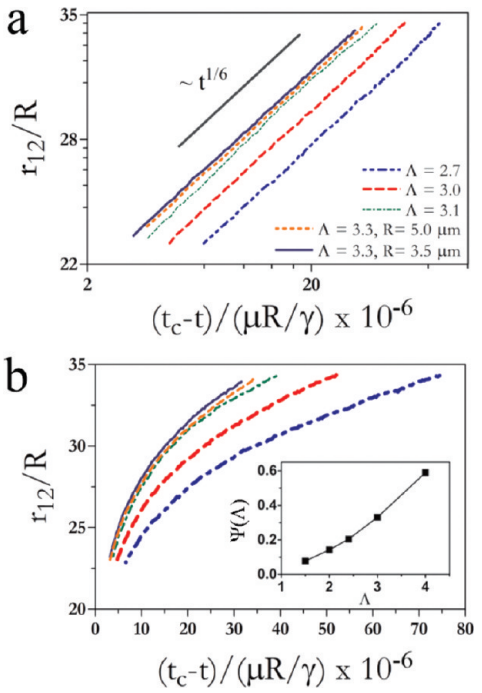

Figure 12. Normalized separation distance r_{12}/R vs normalized time to contact $(t_c-t)/(\mu R/\gamma)$ for cylinders approaching end-to-end. (a) The experimental data obey a power-law with exponent in agreement with far-field quadrupolar interactions which gives $r_{12} \sim (t_c - t)^{1/6}$. (b) For fixed Λ, the trajectories approximately superpose. The rate of approach increases with Λ. Inset: Graph of prefactor, $\Psi(\Lambda)$.

we observe the mirror symmetric orientation of the particles (i.e., $\varphi_1 = -\varphi_2$), but not necessarily an end-to-end alignment (i.e., $\varphi_1 = \varphi_2 = 0$). When the separation is on the order of 10 particle radii, the rotation becomes significant and the cylinders align end-to-end, ultimately forming a dimer upon contact. Cylinders that were initially aligned end-to-end maintained this alignment throughout the entire trajectory (see movie in the Supporting Information). Individual cylinders interacting with a preexisting dimer rotate and align coaxially with the dimer. In this way, linear chains of many particles form, all oriented end-to-end. Images of such chains formed by cylinders with $\Lambda = 1.2$ and 2.5 are shown in Figure 1.

In Figure 12a, particle trajectories for pairs of cylinders approaching end-to-end are shown to obey a power law $r_{12} \sim (t_c - t)^{\beta}$ where t is time, and t_c is the contact time for cylinders (determined to within 8 ms). These data span the range $16R < r_{12} < 36R$. The exponent for the data in Figure 12a is $\beta = 0.166 \pm 0.003$. Such a power law had also been reported by Loudet[23] and collaborators for ellipsoids aligned tip-to-tip at fluid interfaces, who showed that this power law is consistent with an interaction energy between polar quadrupoles following $E_{12} \sim r_{12}^{-4}$.[23] (This exponent follows from the balance of capillary force between the polar quadrupoles $F_{12}^{qp} \sim r_{12}^{-5}$ and the viscous drag.[42])

$$F_{12}^{drag} \sim \frac{dr_{12}}{dt}$$

In Figure 12b, particle trajectories are plotted in nondimensional form using the particle radius R to normalize r_{12} and the viscous-capillary time scale $R\gamma/\mu$ to normalize $t - t_c$, where μ is the viscosity of water. This figure shows that curves referring to cylinder assembly events at fixed Λ superpose, and the assembly events are faster with increasing Λ. This can be understood by considering the first term in the far-field expansion to the interaction energy elliptical quadrupoles in eq 15. The prefactor for this term

$$\Psi(\Lambda) = \frac{H_p^2}{R^2}\frac{4\Lambda}{(\Lambda+1)^2}$$

depends on Λ both explicitly and via $H_p(\Lambda)$; this prefactor (shown as the inset to Figure 12) increases monotonically with Λ. Thus, the interaction energies increase in magnitude with Λ for a given r_{12}. The rate of assembly therefore also increases.

By equating the work done by the capillarity to viscous dissipation in the fluid, the interaction energy can be estimated directly. The viscous dissipation is[43,44]

$$\Delta E_{12}^{Diss} = -\int_{r_1}^{r_2} F_{drag}\, dr_{12} = 6\pi\mu R C_D(\theta_C,\Lambda)\int_{r_1}^{r_2} v_{12}\, dr_{12} \qquad (20)$$

where v_{12} is the instantaneous particle velocity and $C_D(\theta_C,\Lambda)$ is a drag coefficient which can account for particle geometry and orientation.[45] Since the particle is only partially immersed, the drag coefficient also depends upon wetting conditions and degree of immersion. We calculate ΔE_{12}^{Diss} for three of the data sets reported in Figure 12, for which $\Lambda = 3.1 \pm 0.1$, $R = 5.0\,\mu$m, $r_1 = 16R$, and $r_2 = 36R$, using centered differences to compute v_{12} from r_{12} versus t. In these experiments, we report end-to-end attraction, so the drag on cylinders occurs only in the axial direction. Evaluation of eq 20 yields

$$\frac{\Delta E_{12}^{Diss}}{C_D(\theta_C,\Lambda)} = (2.16 \pm 0.65) \times 10^5 kT$$

To complete this estimate, it remains to specify the appropriate value for the drag coefficient, which has not been reported, to our knowledge, for partially immersed cylinders at interfaces. For a completely immersed cylinder which is translating along its major axis, drag coefficients are known, and $C_D \cong 1.73$ for $\Lambda = 3$.[46−48] The cylinders are not fully immersed; the wetted surface area fraction is calculated from numerical simulation to be roughly 60% for the relevant Λ and θ_c. Following Danov and collaborators,[42] who reported a drag coefficient which increases with degree of particle immersion for spherical particles at free surfaces, we weight C_D with wetted surface area. Thus, the estimate for viscous dissipation $\Delta E_{12}^{Diss} \cong (2.24 \pm 0.67) \times 10^5 kT$. The corresponding change in capillary energy between elliptical quadrupoles calculated from eq 20 for the same range of center to center distances is $\Delta E_{12}^{ee} = 9.85 \times 10^4 kT$, within a factor of $O(1)$ from the measured viscous dissipation. For this calculation, we set

(42) For the microparticles studied, the Reynolds number $Re = \rho_p v_{12} R/\mu$ and the capillary number $Ca = \mu v_{12}/\gamma$ are negligible, so both inertia and viscous deformation of the interface can be neglected. In this limit, drag on the particle can be calculated according to eq 20.

(43) Danov, K. Aust, R. Durst, F. Lange, U. *J. Colloid Interface Sci.* **1995**, *175*, 36−45.
(44) Petkov, J. T.; Danov, K.; Denkov, N. D.; Aust, R.; Durst, F. *Langmuir* **1996**, *12*, 2650−2653.
(45) This definition of the drag coefficient is appropriate for particles with moderate aspect ratios (see eq 4−30.11 in ref 46) such as those studied in our experiments. For very elongated particles, a drag coefficient $\hat{C}_d$ can be defined as $F_{drag} = -2\pi\mu L v_{12}\hat{C}$. This form for $\hat{C}_d = 1/(\ln\Lambda + 0.19315)$, which varies slowly with aspect ratio. (see eq 4−31.4 in ref 46).
(46) *Low Reynolds number hydrodynamics with special applications to particulate media*, Fifth printing; Happel, J., Brenner, H., Eds.; Kluwer Academic Publishers: Dordrecht, The Netherlands, 1991.
(47) Heiss, J. F.; Coull, J. *Chem. Eng. Prog.* **1952**, *48*, 133−140.
(48) Youngren, G. K., Acrivos, A. *J. Fluid Mech.* **1975**, *69*, 377−408.

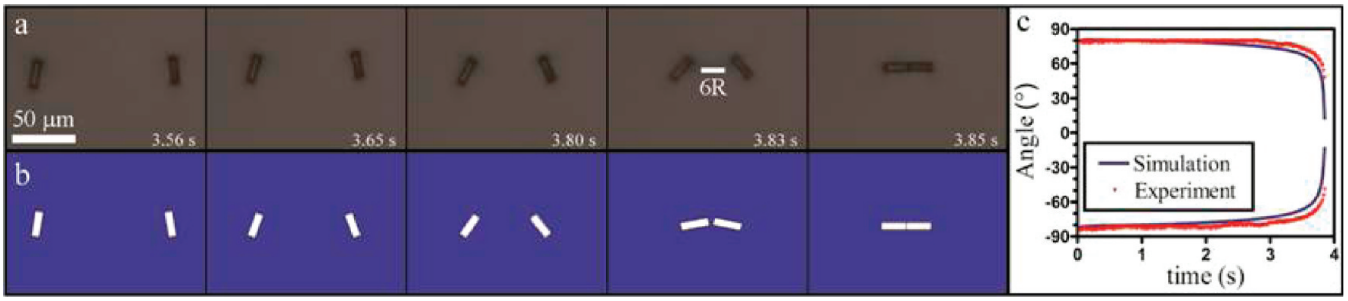

Figure 13. Interacting, rotating cylinders with $L = 21$ μm and $R = 3.5$ μm. Sequence of images from (a) experiment (top row) and (b) numerical prediction using the elliptical pair potential (bottom row). The simulation is initialized with the experimental values of φ_1 and φ_2 measured at $r_{12} = 34R$, for which $t = 0$. (c) Angular orientation of each particle as a function of time. Experiment (red triangles). Prediction (blue line).

the quadrupole amplitude to $H_p = 0.66R$, which is inferred from Figure 11 for $\Lambda = 3$.

3.3.2. Comparison of Experimental and Predicted Dynamics. The pair potential is used here to describe the dynamics of particle approach for a case in which the particles, initially in aligned nearly side-to-side, co-rotate in mirror symmetry to assemble end-to-end. In Figure 13a, we present several frames from an experiment (top row) and corresponding frames from a dynamic simulation (bottom row) based on the analytical pair potential. In the experimental images, owing to the limited time resolution of the camera, there are some experimental uncertainties for the fourth frame (~16 ms from contact). The simulations were performed assuming quasistatic migration and assuming a diagonal mobility matrix, so rotation and translation are hydrodynamically decoupled. The simulations were initiated with known r_{12} and bond angles. Positions and bond angles were updated via an explicit Euler scheme using the analytical expressions for E_{12}:

$$r_{12}^{n+1} = r_{12}^{n} - \frac{\Delta t}{6\pi\mu R C_D}\left(\frac{\partial E_{12}}{\partial r_{12}}\right)^n \tag{21a}$$

$$\varphi_i^{n+1} = \varphi_i^{n} - \frac{\Delta t}{\pi\mu L^3 C_D^*}\left(\frac{\partial E_{12}}{\partial \varphi_i}\right)^n \tag{21b}$$

where the superscripts n and $n+1$ refer to the nth and $(n+1)$th time steps, and φ_i is the bond angle of the ith particle, where $i = 1, 2$. We initiate the simulation 3.85 s before contact; to do so, we extract the initial conditions for the bond angles from the corresponding experimental frame. The sole free parameters in this simulation are the drag coefficients for rotation and translation, denoted C_D and C_D^*, respectively; these parameters are obtained by fitting the experimental results. The best fit drag coefficient to translation $C_D \approx 0.53$. The best fit drag coefficient to rotation $C_D^* \approx 0.09$. These values are a fraction of those expected for an elongated particle in the bulk.[49] Although there is significant theoretical work[53] and experimental work[54,55] for rods at fluid−fluid interfaces having $\Lambda \gg 1$, experiment and theory addressing rotational drag at interfaces for cylinders with moderate Λ is lacking. Hence, we use the fitted value.

The particles attract each other in mirror alignment until they are quite close; they then rapidly co-rotate to end-to-end alignment. Note that much of this rotation occurs for particle separations greater than $6R$ (as indicated in the figure). Thus, this rotation occurs for interactions in the outer domain. For this reason, the torque which drives the co-rotation is well captured by the pair-potential. The instantaneous predicted bond angles for both particles are compared to those in experiment in Figure 13b. The ability of the pair potential to resolve the rotation underscores the importance of the pair-interactions in the outer domain, which drive the rotation over distances where the concentrated excess area in the inner domain cannot play a role.

3.4. Near Field Effects: A Capillary Bridge. The pair potential of interactions captures the dynamics of interaction, in particular the observation that cylinders approach in stable end-to-end alignment or corotate to that alignment. It also predicts that end-to-end orientations are favored for $r_{12} \geq \sqrt{2}(L)$ and that side-to-side assembly is favored for closer approach. This latter prediction is not consistent with the end-to-end chaining observed in experiment for cylinders. The pair potential does not include interactions in the inner domain owing to the near-field excess surface area density near the cylinder end face. The elimination of this near-field excess area would contribute significantly to the energy reduction for cylinders near contact, thereby preventing rotation from end-to-end alignment at close approach. We suggest that for close approach, the deformation fields overlap to create a capillary bridge, and that bending or deformation of this bridge creates an energy barrier preventing rotation to the side-to-side configuration. Preliminary simulations of a capillary bridge between cylinders aligned end-to-end (neglecting rotation of the major axis with respect to the plane of the interface) are shown in Figure 14. Rotation would strain this "bridge" leading to a restoring torque, as shown schematically in the inset. This is a subject of ongoing research.

3.5. Lattice Structures. Up to now, we have discussed cylinders in isolation, and the tendency for cylinders to chain. On crowded surfaces, cylinders form lattices upon assembly. An image of a dense structure at the interface of a water drop in hexadecane is shown in Figure 15. These structures form spontaneously upon gentle shaking of a vial containing water, hexadecane, and cylindrical particles. The structured domains cover the surface area of the drop, forming a colloidisome, or droplet

(49) For immersed particles, C_d^* is function of aspect ratio and depends on the exact geometry of the particle for a given Λ. For a completely immersed ellipsoid, an analytical solution is available which gives $C_d^* = 0.26$ for $\Lambda = 3$.[50] Simulations of immersed right circular cylinders[51] yield $C_d^* \cong 0.69$ for $\Lambda = 2.04$ and $C_d^* \cong 0.40$ for $\Lambda = 3.4$. Interpolation formulas, developed by Garcia de la Torre and coworkers,[52] yield $C_d^* \cong 0.45$ for a cylinder with $\Lambda = 3.0$.

(50) Kim, S.; Karrila, J. *Microhydrodynamics, Principles and Selected Applications*; Butterworth-Heinemann: Boston, MA, 1991.

(51) Allison, S. *Macromolecules* **1999**, *32*, 5304–5312.

(52) Tirado, M. M.; Martinez, C. L.; Garcia de la Torre, J. *J. Chem. Phys.* **1984**, *81*, 2047.

(53) Reynaert, S.; Brooks, C. F.; Moldenaers, P.; Vermant, J.; Fuller, G. *J. Rheol.* **2008**, *52*, 261−285.

(54) Levine, A. J.; Liverpool, T. B.; MacKintosh, F. C. *Phys. Rev. E* **2004**, *69*, 021503.

(55) Lee, M. H.; Lapointe, C. P.; Reich, D. H.; Stebe, K. J.; Leheny, R. L. *Langmuir* **2009**, *25*, 7976–7982.

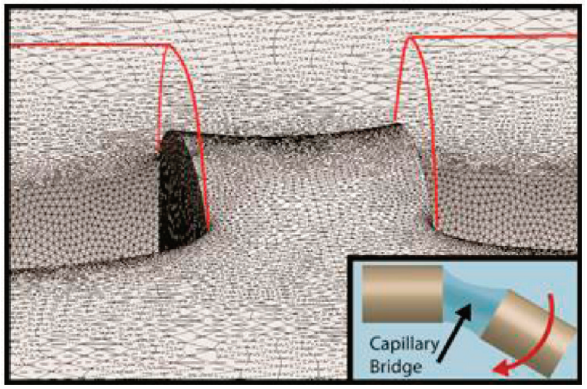

Figure 14. Numerical simulation of interface topography between two particles which form a capillary bridge. Inset: Schematic of strained capillary bridge owing to rotation from end-to-end alignment.

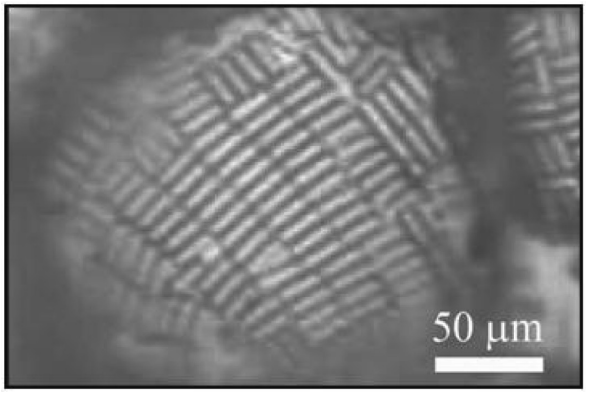

Figure 15. Lattice of cylinders formed spontaneously on the interface of a water drop in hexadecane ($\Lambda = 2.4$ and $\theta_c = 130°$).

stabilized by adsorbed colloidal particles. This colloidisome differs significantly from others which have appeared in the literature, which include colloidisomes formed form densely packed spherical particles with interesting packing defects,[56] 'hairy' colloidisomes formed from long, slender, needle-like rods,[57] and colloidisomes formed from ellipsoidal particles which form open, triangular-like structures.[31]

The cylinders form a regular, rectangular lattice of cylinders aligned both end-to-end and side-to-side. We speculate that the contact line along a row of cylinders is wavy, with a wavelength related to the particle dimension. The observed alignment might be understood in terms of arguments proposed by Lucassen, who studied the rate of decay of interactions between wavy contact lines in the small slope limit.[19] Lucassen's analysis showed that surface energy associated with deformations created by wavy contact lines decays exponentially with a decay length related to the wavelength of the feature, and that these interactions are attractive for undulations that are in phase, promoting assembly of features in registry. Grain boundaries in the structures are also evident, where the cylinders form dense lattices aligned perpendicular to the larger domain. The formation of these organized, closely packed structures is a subject of ongoing study in our group.

(56) Dinsmore, A. D., Hsu, M. F., Nikolades, M. G., Marquez, M., Bausch, A. R., Weitz, D. A. *Science* **2002**, *298*, 1006−1009
(57) Noble, P. F., Cayre, O. J., Alargova, R. G., Velev, O. D. Paunov, V. N. *J. Am. Chem. Soc.*, **2004**, *126*, 8092−8093.

4. Conclusions

In this paper, we report on the behavior of cylindrical microparticles at interfaces in isolation, in interaction and in dense assemblies.

We derive an anisotropic interaction potential appropriate to understand interactions between elongated particles based upon interacting elliptical quadrupoles. The potential predicts forces on particles. Notably, the potential also predicts torques which drive preferred alignment during approach and upon assembly. The forces and torques depend strongly on particle aspect ratio. This pair potential is evaluated for parameters relevant for interacting cylinders, but is generically useful to describe interactions of any elongated particles.

We describe right circular cylinders at fluid interfaces using theory, experiment, and supporting numerics. A phase diagram relating contact angle and aspect ratio predicts the configuration of an isolated cylinder at a fluid interface. The data suggest that the surface energy term related to the "hole" in the interface provides the largest contribution and determines whether a cylinder will lie end-on or side-on. The predicted orientations are observed in experiment, as are metastable states of adsorbed cylinders at aqueous−oil interfaces. Side-on cylinders create deformation fields as the interface bends to satisfy its wetting conditions. Comparison of experimentally obtained interface topographies to numerical predictions based on minimum surface free energy configurations confirms that the interfacial deformation around isolated cylinders is determined by capillarity. The deformation field is well described by an elliptical quadrupole for distances greater than a few radii from the cylinder surface.

In interaction on dilute surfaces, side-on cylinders form chains. The anisotropic interaction potential based on interacting elliptical quadrupoles explains the preference for end-to-end alignment prior to chaining. Trajectories for pairs of interacting particles approaching end-to-end agree with the predicted force. Also in agreement with prediction, the cylinders approached faster for greater aspect ratios. The trajectory for a pair of interacting cylinders initially aligned side-to-side compares favorably to the predicted rates of rotation; the particles co-rotate in mirror-symmetric orientations to chain end-to-end. Stable end-to-end chaining is likely enforced by near field interactions. Numerical simulations reveal that excess surface area density is concentrated in a region quite close to the cylinder end faces. Near contact, these areas of high excess surface areas overlap to form a capillary bridge which may enforce stable end-to-end chaining. On crowded surfaces, cylinders pack to form densely packed rectangular lattices on oil−water interfaces to form colloidosomes. The regular structure of the particles on the colloidosomes, and their dense packing differ from assemblies formed by spheres, needle-like particles and ellipsoids.

Acknowledgment. The contributions of J. Crocker for developing the interferometric setup and methods, A. Tseng for assistance with the environmental SEM images, and the Penn Regional Nanotechnology Facility at the University of Pennsylvania for shared facilities are gratefully acknowledged.

Supporting Information Available: Text discussing the determination of interaction energy between elliptical quadrupoles, a figure showing a comparison of the elliptical pairwise potential with the numerical simulation and a video of trajectories of interacting pairs of cylinders recorded at aqueous−air interfaces using video microscopy. This material is available free of charge via the Internet at http://pubs.acs.org.